Augmented and quenched local moments in a van der Waals itinerant moiré ferromagnet

Saransha Mohanty [1], Weibo Gao,[2] and Pritam Deb[1,*]

[1]*Department of Physics, Tezpur University (Central University), Tezpur-784028, India*

[2]*Division of Physics and Applied Physics, School of Physical and Mathematical Sciences, Nanyang Technological University, Singapore 639798, Singapore*

(Received 15 March 2023; revised 10 August 2023; accepted 11 August 2023; published 23 August 2023)

Twisted two-dimensional (2D) van der Waals (vdW) quantum materials are renowned for their uncanny features like unconventional superconductivity, metal insulator transition (Mott transition), spin liquid phase etc., offering a rich landscape for strong electron correlations. Such electronic correlations also account for unusual magnetism in twisted crystals. However, advancement in the field of 2D twisted magnetism has been constrained, owing to lack of ideal materials as well as proper ways to design moiré magnets correlating their emergent magnetic and electronic properties. Here, we design a vdW moiré magnet and demonstrate that the simple act of rotating two monolayers i.e., 1T-$NbSe_2$ and 1T-VSe_2 at various twist angles, produces an inhomogeneous mixture of augmented and quenched localized magnetic moments per transition metal vanadium (V) and niobium (Nb) atoms. Precisely, twist angle affects the induced local magnetic moments of each constituent layers. Notable flat bands and itinerant ferromagnetism emerge in vdW moiré superlattice, the latter satisfying Stoner criterion. These features result from orbital rehybridization at atomic lattice sites instead of interlayer coupling between layers. Moreover, orbital magnetism is identified in untwisted heterobilayer system. The results present an effective strategy for designing moiré magnets with insights into new quantum-mechanical phenomenon of twist regulated on-site magnetism.

DOI: 10.1103/PhysRevB.108.054433

I. INTRODUCTION

Moiré superlattice emerges when two crystal sheets undergo a relative shift in terms of atomic positions with a twist angle [1–3]. Twisted crystal lattices have periodic electron density rearrangements and elongated lattice parameters. Moiré superlattice in twisted crystal sheets induces strong electron-electron (e^--e^-) interactions, unlike non-twisted ones, ensuing a broad array of electronic properties such as the Hofstadter Butterfly effect, superconductivity, noncollinear phases, and large anomalous Hall Effect which are significant for cutting edge technologies as well as having direct impact on fundamental research [4–16]. It is a matter of fact that these electronic correlations are also important for manifestation of magnetism in twisted layered solids. While the discovery of superconductivity at a twist angle 1.1° of bilayer graphene has prompted new research thrust in the field of twistronics, understanding and reporting the emergence of magnetism in twisted layers has remained as unmet challenge in low dimension. Two-dimensional (2D) crystals can follow any of these cases: (i) at least two nonmagnetic materials (NM) with a relative rotational angle to each other; (ii) at least two magnetic [e.g., combination of ferromagnet (FM)/antiferromagnet (AFM)] materials; and (iii) one nonmagnetic (NM) and one magnetic material, respectively, with a twist to exhibit magnetism [17–29].

One of the prominent electronic features of twisted 2D crystals is the appearance of flat bands in dispersion relations at Fermi level. A few examples correlating flat bands with magnetism have been reported in the basket weave lattice (e.g., kagome magnets) family and graphene twisted layers (GTLs). The kagome magnet $Co_3Sn_2S_2$ has shown a negative flat band mechanism whereas GTLs have exhibited unusual magnetotransparent properties [30–38]. The origin of all such effects can be enrooted to robust localization of electrons or strong spin-orbit coupling in twisted layers [39–43]. Despite such success, rapid advancements in 2D twisted magnetism have been impeded by the challenge of identifying appropriate materials and a suitable approach to create moiré magnets correlating their emergent magnetic and electronic properties. Hence, unveiling these moiré magnets is crucial for the expansion of new technologies and science.

In this manuscript, we design a moiré ferromagent with twisted geometry of 1T-$NbSe_2$/1T-VSe_2 monolayers and explore its emergent electronic properties. Ferromagnetism in pristine monolayer 1T-VSe_2 has been the subject of intense research in recent years. It is due to the fact that VSe_2 monolayer exhibits both ferromagnetism with high Curie temperature (T_C) value (∼330 K), and a charge density wave (CDW) phase in the transition temperature (T_{CDW}) range of 15–150 K [44,45]. Moreover, at very low temperature range up to 6 K, a competition between intrinsic ferromagnetic and antiferromagnetic states is observed in the monolayer limit of VSe_2, where ferromagnetism dominates when combined with other crystals through van der Waals interactions [46]. Nonetheless, in recent years, both theoretical and experimental

*Corresponding author: pdeb@tezu.ernet.in

advances based on vdW systems such as VSe_2/WSe_2, 1H-$NbSe_2$/1T-VSe_2, VSe_2/Bi_2Se_2, VSe_2/WS_2, VSe_2/graphene, and 1T-$MoSe_2$/1T-VSe_2/2H-WSe_2/1T-VSe_2/1T-$MoSe_2$ as 2D magnetic tunnel junctions and 1T-VSe_2/ BiFeO3(0001) etc., have considered the ferromagnetic nature of monolayer VSe_2 for real time spintronic devices [47–53]. Similarly, pristine 1T phase of $NbSe_2$ monolayer is a non-magnetic (NM) metal [54]. Experimental reports have confirmed the existence of a stable 1T phase in both $VSe_2$and $NbSe_2$ monolayers [44,54]. By considering the above two materials, we report an interesting manifestation of on-site magnetic moment fluctuations with amplified and dampened local moments in transition metal atoms (Nb, V) upon twisting. We find magnetic moments of the VSe_2 and $NbSe_2$ layers become nonuniform by virtue of the twist angles. Specifically, larger twist angles give rise to a substantial fluctuation of local moments. Furthermore, nonmagnetic $NbSe_2$ monolayer is weakly magnetized in both twisted and nontwisted forms together with emergence of pronounced flat bands near Fermi level at every twisted angle. By conducting *ab initio* calculations, we investigate the cause of such distinctive features exhibited by the twisted metal vdW heterobilayers. Additionally, incorporating maximally localized Wannier function (MLWF) in the untwisted configuration, we find evidence of orbital magnetism in the system. Both vanadium (V) and niobium (Nb) atoms contribute toward spin and orbital magnetism in structures studied. The findings provide an excellent demonstration of the interplay between high electron correlations, emergent magnetism, and flat bands generated from atomic rearrangements, exhibiting impressive twist-angle monitored ferromagnetism.

II. COMPUTATIONAL DETAILS

Ground state electronic properties of the 1T-$NbSe_2$/1T-VSe_2 vdW heterobilayer are investigated using the Perdew-Burke-Ernzerhof (PBE) exchange-correlation functional with generalized gradient approximation (GGA) as coded in Quantum Espresso (QE) [55]. The slab model of system is constructed using 30 Å vacuum along the 001 direction (i.e., z direction), to prevent periodic image interactions between the neighboring layers. We sample the Brillouin zone (BZ) for nontwisted geometries with a $12 \times 12 \times 1$ k-points grid. The twisted unit cells are sampled with a $4 \times 4 \times 1$ unshifted k-points mesh, whereas only the Γ point is considered for atoms more than 150 in moire cell. The pseudopotentials are considered from the solid-state pseudopotentials (SSSP) library [56]. The bilayer nontwisted cell is relaxed with a force convergence of 10^{-7} Rydberg (Ry), and the full relaxation criteria is achieved up to 10^{-3} Ry for twisted crystal lattices by considering a 1633 eV and 544 eV cut of energy for Kohn-Sham (KS) wave functions, respectively. Charge density cut off values are six times larger than cut of energy in each case. We implement DFT-D van der Waals (vdW) corrections between two monolayers as well as the Broyden-Fletcher-Goldfarb-Shanno (BFGS) algorithm in optimization of the slab model. The effect of strong onsite coulombic repulsion is studied using Hubbard U parameters with values 2.95 eV and 2 eV for Nb and V atoms. We find spin-orbit coupling and Hubbard U effects are negligible after a careful analysis of electronic properties (Fig. S1 of the Supplemental Material [57]). Therefore, these effects are not considered in subsequent calculations. Information regarding moiré lattice constant, strain, relaxed interlayer separations, total number of atoms, and total magnetic moments are provided in Sec. A of the Supplemental Material [57]. We choose V(d), Nb(d), and Se(p) orbitals for wannierzation of the nontwisted bilayer system. Calculations are carried out by incorporating Wannier90 code and WannierTools with a dense $400 \times 400 \times 1$ interpolation grid orbital magnetization [58,59].

III. RESULTS AND DISCUSSIONS

A van der Waals heterostructure can be fabricated in several ways on account of different stacking orders, relative orientations within layers, and material functionalities. Out of many possibilities, we consider a nontwisted AA stacked heterostructure constructed out of monolayers (mLs) belonging to the transition metal dichalcogenides (TMDs) family and the corresponding effective moiré unit cells at various twist angles. The heterobilayer is composed of a trigonal phase of nonmagnetic metal (nMm) $NbSe_2$ and metal ferromagnet (mF) VSe_2monolayers. In AA stacked heterobilayers, the nMm $NbSe_2$ single crystal layer lay on top of the VSe_2 monolayer in such a way that their lateral atomic sites coincide and appear as a single sheet of crystal atoms [see Fig. 1(a)], when viewed from the top (bottom). Both the 1T-$NbSe_2$ and 1T-VSe_2 monolayers belong to space group $P\bar{3}m1$ with lattice constants 3.52 Å and 3.43 Å [60]. In the model heterobilayer, the optimized lattice constant is $a = 3.48$Å with lattice mismatch of $\leqslant 2\%$.

Figure 1(b) displays a side profile of an AA stacked heterostructure with relaxed interatomic distance of 3.09 Å.The twisted configurations are designed using the coinciding site lattice (CSL) point method [61–63]. Figures 1(c)–1(e) represent development of commensurate moiré lattices of AA stacked heterostructures at three relative rotational angles with zero strain. To construct moiré unit cells with CSL, a set of two integers (n, m) is required. The equation relating vector components n, m to the moiré superlattice vector is given by $V_{\text{moire}} = nX + mY$, where lattice vectors X and Y correspond to constituent monolayers. In our case, with $n = 7$ and $m = 6$, twisted configurations contain 114, 42, and 78 atoms at twist angles(θ) 13.17°, 21.79°, and 27.80°, respectively. The underlying equation $\cos\theta = \frac{1}{2}\frac{n^2+m^2+4nm}{n^2+m^2+nm}$ correlates n and m with twist angle (θ) [64,65]. The configurations have the formation energies ($E_{\text{formation}}$) −115 meV, −32 meV, −32 meV, and −31 meV per atoms, respectively, in increasing order of twist angles from 0° to 27.80° at optimized distances, following the relation, $E_{\text{formation}} = (E_{\text{hetero}} - E_{VSe_2} - E_{NbSe_2})/N$, where E_{hetero}, E_{VSe_2}, and E_{NbSe_2} represent total energy of bilayer as well as monolayer systems, respectively, with N as the total number of atoms in the heterostructure. Herein, all our calculations are carried out at fully relaxed interlayer separations d_{relaxed} between the two layers, which correspond to metastable states. These are the interlayer separations d_{relaxed} where induced magnetism is the strongest. Induced magnetic moments with interlayer distance are plotted in Fig. S2 of the Supplemental Material [57].

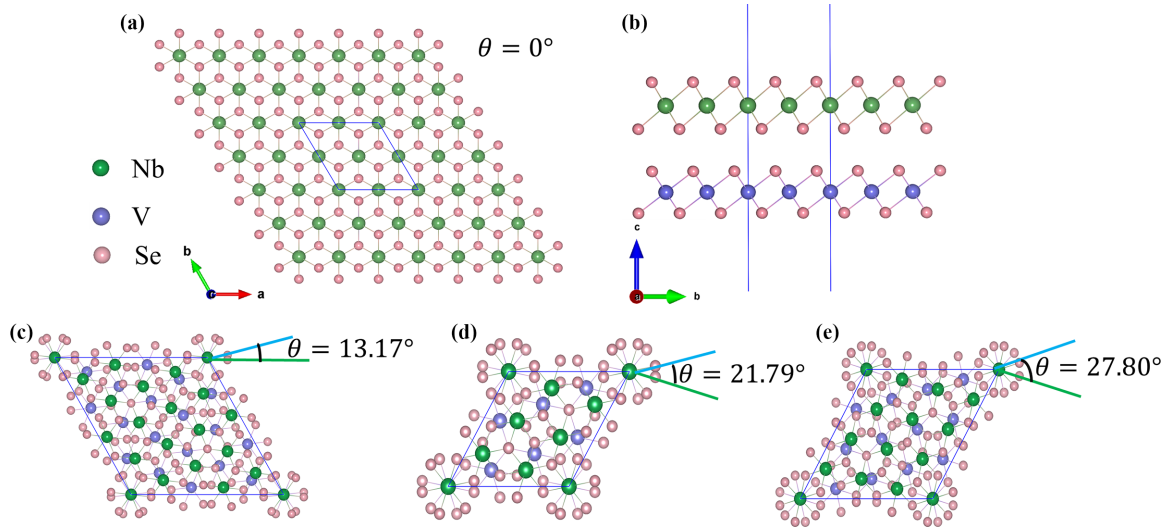

FIG. 1. Portrayal of atomic configurations for optimized vdW moiré magnets. (a) Upper view of extended AA stacked 1T-$NbSe_2$ and 1T-VSe_2vdW heterobilayers; (b) lateral view of bilayer heterostructure, top view of twisted unit cells at (c) $\theta = 13.17^\circ$, (d) $\theta = 21.79^\circ$, and (d) $\theta = 27.80^\circ$ (Blue, green, and light pink spheres represent vanadium, niobium, and selenium atoms, respectively).

The moiré unit cells so obtained induce electron density reconfigurations at lattice sites owing to atomic rearrangements as depicted in Figs. 2(a)–2(d). The change in distributions of overlap electron density zones owing to atomic reconstructions with respect to twist angles is highlighted in Figs. 2(a)–2(d). In comparison to nontwisted counterparts [see Fig. 2(a)], twisted geometry causes a variation in electron density concentrations at distinct atomic lattice positions. In Fig. 2(a), the central Nb atom seems to be surrounded by six Se atoms with alternate high and low density zones, indicating a well-distributed periodic overlap regime of electron density. The orbital overlap regions of electrons fluctuate according to the rearrangement of atoms within unit cells with twist angles. In twisted cells, dense orbitals overlap

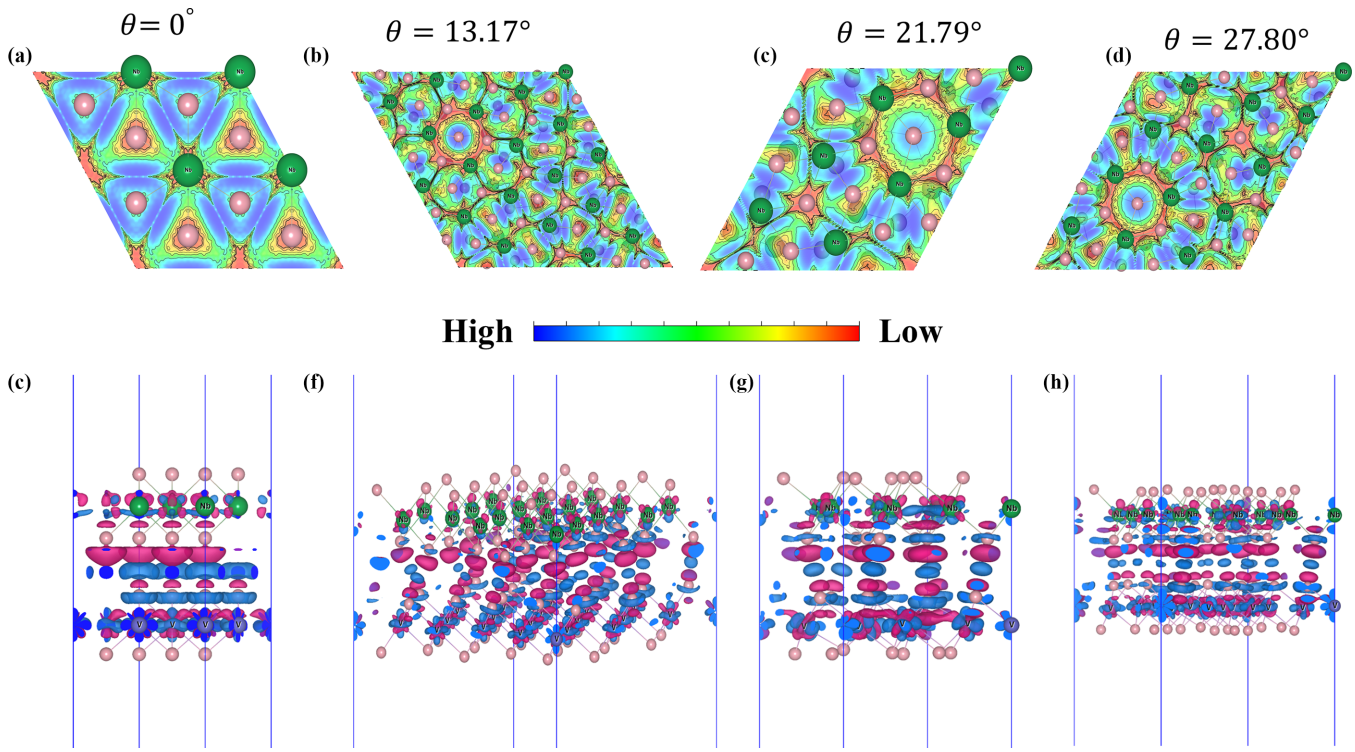

FIG. 2. Density overlap region and charge density difference (CDD) analysis of moiré magnets. First row (a)–(d) displays contour plot of density overlap regions at the interface along with a lateral view of CDD plots (e)–(h) in the second row for vdW $NbSe_2$-VSe_2 hybrid systems with isosurface value of 0.0004 electron/Å. Blue and Red lobes represent net charge accumulation and dissipations across the layers and at atomic sites, respectively. (Color box shows maximum and minimum density overlap regions indicated by blue and red color).

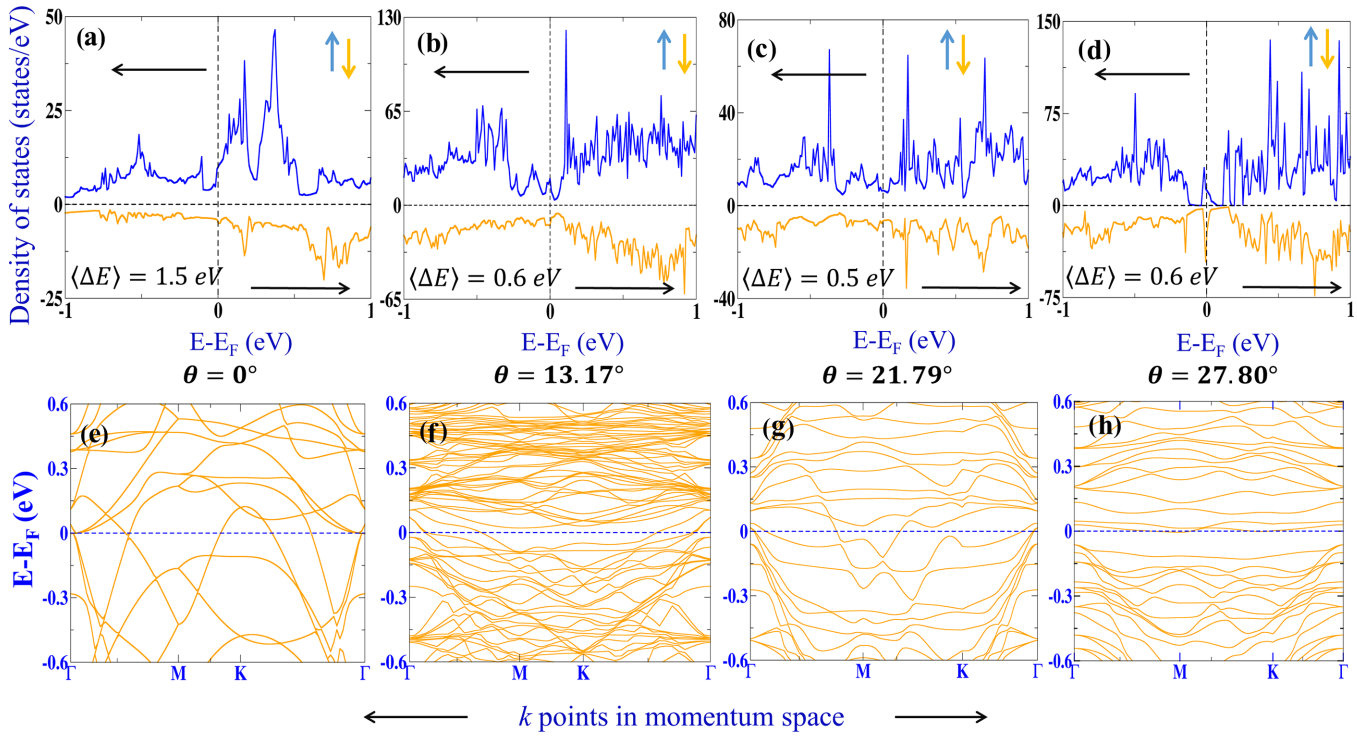

FIG. 3. Illustration of spin populations under spin polarized density of states (DOS) (a)–(d) and energy spectrum diagrams (e)–(h) for spin up channel at twist angle $\theta = 0°$, 13.17°, 21.79°, and 27.80°. The black arrows in the DOS plot correspond to shuffle of density peaks for spin up (blue arrow) and down channels (orange arrow) toward valance band (VB) and conduction band (CB) regions with respect to Fermi energy under spin polarization. Here, $\langle \triangle E \rangle$ corresponds to average exchange splitting energy in the energy range of -1 eV to 1 eV.

domains arise with an increase in the number of atoms, as shown in Figs. 2(b)–2(d). Color differences indicate that high densities (blue) appear closer to Nb (V)-Se and Se-Se atoms in close proximity, and low densities (pink/red) appear when they are far apart [66]. The orbital overlap region at interface promotes interfacial charge accumulations or depletions and has become apparent in subsequent discussion on charge density difference plots. The Charge density difference (CDD) mechanism accounts for charge redistributions at interface as well as at atomic sites when heterostructures are formed. Mathematically, $\rho_{\text{differnece}}(\vec{r}) = \rho_{\text{hetero}}(\vec{r}) - \rho_{VSe_2}(\vec{r}) - \rho_{NbSe_2}(\vec{r})$, where $\rho_{\text{differnece}}(\vec{r})$ is the difference of charge densities, $\rho_{\text{hetero}}(\vec{r})$, $\rho_{VSe_2}(\vec{r})$, and $\rho_{NbSe_2}(\vec{r})$ are charge density of heterobilayer and corresponding monolayer system. At the interface of all configurations, a charge accumulation layer appears which is sandwiched between two alternative depletion layers originating from two nearest atomic planes of selenium (Se) atoms, belong to VSe_2 and $NbSe_2$ monolayers. The charge gain at interface imply emergence of hybridization in considered heterobilayers. For twisted layers, nearly identical charge gain at the interface is observed owing to comparable formation energies in the moiré unit cells, whereas with higher formation energy for twist free heterobilayer, a relatively high accumulation of charges is noticed; see Fig. 2(e). Also, a small charge redistribution is observed at V and Nb atomic sites, represented in separate planar averaged charge density difference plots in Fig. S3 of the Supplemental Material [57]. The CDD analysis discloses redistribution of charge occurs at both interlayer and intralayer regions upon twisting. The top view CDD is attached in Fig. S4 of the Supplemental Material [57]. The charge distributions closely follow the moiré patterns obtained in all studied configurations. The work functions (WF) for VSe_2, $NbSe_2$, and twist free $VSe_2/NbSe_2$ layers are found to be 5.14 eV, 4.43 eV, and 4.47 eV, respectively. The work function value of VSe_2 monolayer here is really close to the experimentally reported value of 5.52 eV [67]. The potential profiles for all twisted cells (with WF= 4.76 eV) remain relatively the same as depicted in Fig. S3 of the Supplemental Material [57]. A similar case is also identified in twisted MoS_2/ layers [63]. However, the potential drop of approximately 11 eV in both twist free and twisted layers reflect the appearance of built in electric fields. These inbuilt electric fields in all unit cells could facilitate charge separations at the interface and within the layers. This might be the reason we have observed such variations of charge density lobes at both interlayer and intralayer regions. In the bilayer system, potential depth of $NbSe_2$ is higher than the VSe_2 monolayer system. It suggests, global charge transfer can take place from the VSe_2 to $NbSe_2$ layer [68,69]. The planar average charge density difference plots reflect the strength of charge distributions and are found to be small, reflecting weak interlayer coupling. The work function plots are displayed in Fig. S5 of the Supplemental Material [57].

Under spin polarization, majority electron density peaks migrate toward (black arrows) the lower energy area (Valance band region) while minority charge carrier density peaks shift into the conduction band region (high energy zone) compared to unpolarized DOS for each configuration (see Fig. S6 of the Supplemental Material [57]), creating an exchange splitting

TABLE I. Stoner criterion at four investigated configurations.

Twist angle (θ°)	$M_t(\mu_B)$	$\langle\Delta E\rangle$(eV)	I (eV)	$n^\circ(E_F)$states/eV	$I\times n^\circ(E_F)$
0°	6.8	1.5	0.22	18.65	4.1
13.17°	14.32	0.6	0.04	40.54	1.6
21.79°	7.3	0.5	0.067	15.74	1.05
27.80°	13.79	0.6	0.04	65.95	2.6

of atomic orbitals, as shown in Figs. 3(a)–3(d). The average exchange splitting energies $\langle\triangle E\rangle$ are obtained to be 1.5 eV, 0.6 eV, 0.5 eV, and 0.6 eV for bilayer heterostructure and moiré unit cells. Figures 3(a)–3(d) reveal the spin populations are asymmetric, suggesting ferromagnetism with broken time reversal symmetry (TRS). Mostly, *d* orbitals of vanadium (V) and niobium (Nb) atoms are spin polarized. The discussion on orbital indices undergoing exchange splitting is added in Fig. S7 of the Supplemental Material [57]. The nonmagnetic Nb atoms acquire magnetization in both twisted and nontwisted configurations. Moreover, the chalcogen (Se) atoms induce an opposite magnetic moment to that of transition metals Nb (V). Similar effects have been observed in monolayers VS_2 and $FeTe_2$, owing to hybridization between chalcogen X_2 (X = S/Te) *p* orbitals and transition metals M (M = V/Fe) *d* orbitals [70]. In most transition metals, unpaired electrons in *d* orbitals are responsible ferromagnetism, but the nature of the aforementioned emergent magnetism in all considered structures needs to be verified further. Here, we investigate magnetism on the basis of the Stoner model of magnetism in metals [71,72]. The DOS plots proclaim both twisted and nontwisted vdW heterostructure are metal ferromagnets.

The Stoner model explains that magnetism in metals emerges from itinerant electrons aligned in a particular way, exhibiting spontaneous magnetization, otherwise known as itinerant ferromagnetism. To fulfill Stoner criteria of magnetism, one needs to have two key components: (i) stoner parameter or exchange parameter (*I*) and (ii) density of state at Fermi energy $n^\circ(E_F)$. The stoner criteria is satisfied when multiplicative value of exchange parameter (*I*) and DOS at Fermi energy $n^\circ(E_F)$, a unit less quantity, exceeds unity, i.e., $I\times n^\circ(E_F)>1$. In spin polarization calculations the Stoner parameter is related to exchange splitting (ΔE) through the relation $\Delta E = I\times M_t$, where *I* is the exchange integral and M_t is total magnetic moments of transition metal atoms (V and Nb) per cell. The contribution from Se atoms is not considered as they result in antiferromagnetic ordering within the cell. Hence, with two known quantities, M_t and ΔE, exchange parameter *I* can be obtained. All four atomic structures meet the Stoner criterion, making emergent magnetism in bilayer and twisted ones metal ferromagents. Table I lists I, M_t, $\triangle$E, and stoner criterion values. (Detailed Stoner criterion computations and Stoner criterion for total magnetic moments (including chalcogen atoms) are attached inSec. B of the Supplemental Material [57]).

The DOS figures also show the appearance of localized narrow width, sharp peaked electronic densities with twist angle increments. At twist angle 27.80°, density of states is essentially zero before and after Fermi level, implying electrons in both energy ranges have similar energy eigenvalues. This leads to our next introspection on energy band diagrams at both nontwisted and twisted geometry. Figures 3(e)–3(h) display spin up channel energy band diagrams plotted along high symmetry *k* points $\Gamma-M-K-\Gamma$ in the Brillouin zone (BZ) of momentum space. Charge reconfigurations in moiré unit cells provide an extra periodicity to moiré superlattice electrons. Twisted forms have a large density of states due to strong orbital mixing of atoms [see Figs. 3(b)–3(d)]. The induced additional periodicity in twisted geometries modulates the electronic properties; as a result localized states with flat bands have appeared [73,74]. We observe [see Fig. 3(e)] the quadratic nature of electronic bands of nontwisted configuration is transformed into flat bands [Figs. 3(f)–3(h)] with an increase in twist angles. Such phenomenon is represented as flattening of bands. Here, degree of flatness is increasing with the increase in twist angles and more nondegenerate bands start accumulating near Fermi level. The *d* orbital of the V atom contributes more to DOS than Nb-*d* and Se-*p* near Fermi level for nontwisted heterobilayer, which agrees with the projected density of states (PDOS) plot in Fig. 4(a). However, with twist angles, Nb-*d* orbitals (highlighted in blue) dominate near Fermi level compared to V-*d* orbitals [Figs. 4(b)–4(d)] displaying interplay of strong hybridizations between Se-*p*, Nb-*d*, and V-*d* orbitals in vdW twisted layers. Furthermore, the above claim is also supported by orbital resolved band structures in Figs. 4(e)–4(h). Clearly, flat bands near Fermi levels are dominated by the Nb-*d* orbital. At Fermi level, with almost comparable density states, Nb, V, and Se atoms show rehybridization among *d*-*d* and *p*-*d* orbitals, confirming Nb-*d* orbital (green color) supremacy [see Figs. 4(f)–4(h)]. The flat bands near Fermi energy at twist angles $\theta = 13.17^\circ$, 21.79°, and 27.80° are composed of Nb $d_{x^2-y^2}$, d_{z^2}, d_{xy}, V $d_{x^2-y^2}$, d_{z^2}, d_{xy}, and Se p_z orbitals with maximum contributions from Nb atoms, moderately from V, and partially from chalcogen Se atoms [see Figs. 4(f)–4(h)]. The isolated flat band at $\theta = 27.80^\circ$ has emerged from linear recombination of $d_{x^2-y^2}+d_{xy}$ orbitals of Nb atoms. We discern that interlayer surface coupling effect has a minimum impact on flat bands as chalcogen atoms hardly contribute to flatness, revealed from projected band diagrams mentioned above. These features can be attributed to atomic reconstructions in moiré unit cells, similar to cases of twisted transition metal dichalcogenides (TMDs) [75–77]. Separate energy band diagrams for 1T-VSe_2 and 1T-$NbSe_2$ monolayers, as well as orbital contributions toward flat bands, are plotted in Figs. S8, S8A, and S8B in the Supplemental Material, respectively [57]. We observe that V-*d*, Nb-*d*, and Se-*p* orbitals contribute to the overall electronic properties of the respective system.

Induced magnetism of twisted crystals is likewise affected by rearrangement of atoms, depicted in Fig. 5. Figures 5(a)

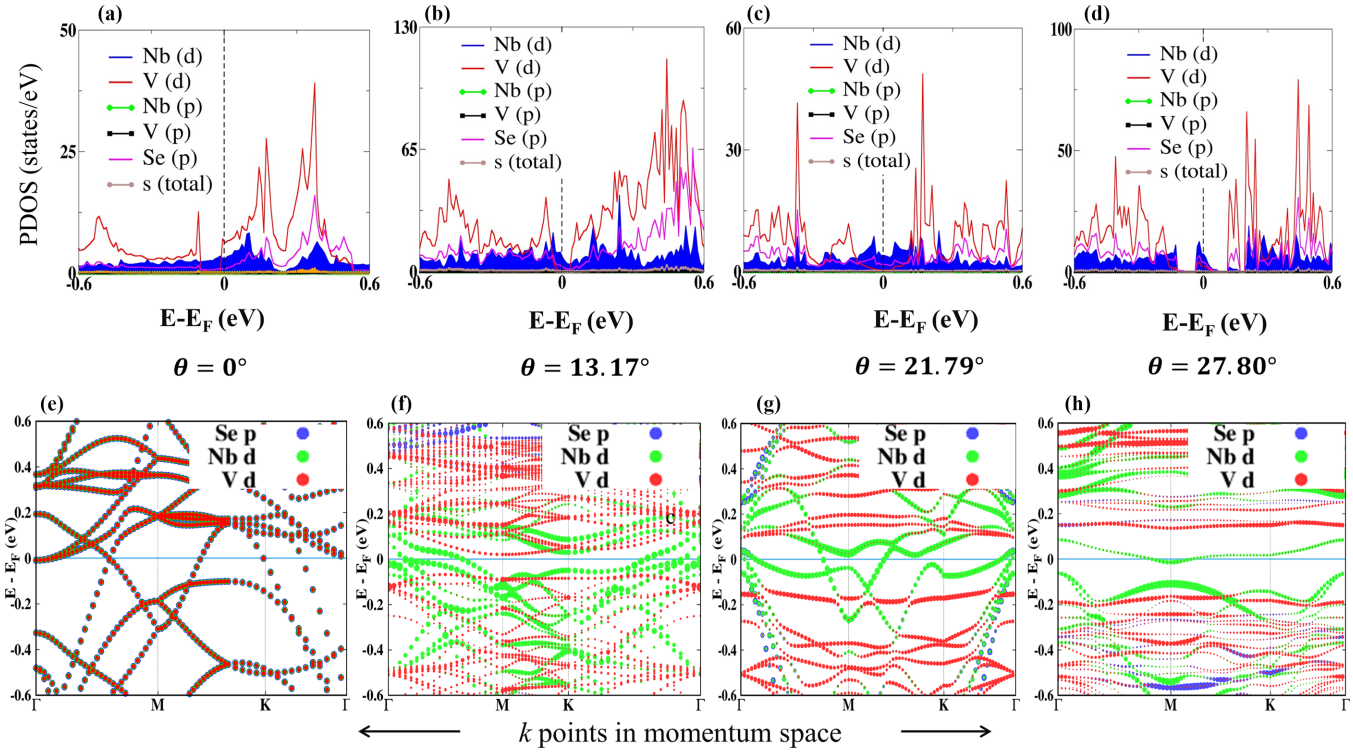

FIG. 4. Representation of projected DOS (PDOS) (a)–(d) and orbital resolved band diagrams (e)–(h) of 1TNbSe$_2$-1TVSe$_2$ vdW heterostructure along $\Gamma - M - K - \Gamma$ directions at $\theta = 0°$ 13.17°, 21.79°, and 27.80° geometrical configurations. Each color in the PDOS plot corresponds to a specific orbital belonging to constituent atoms.

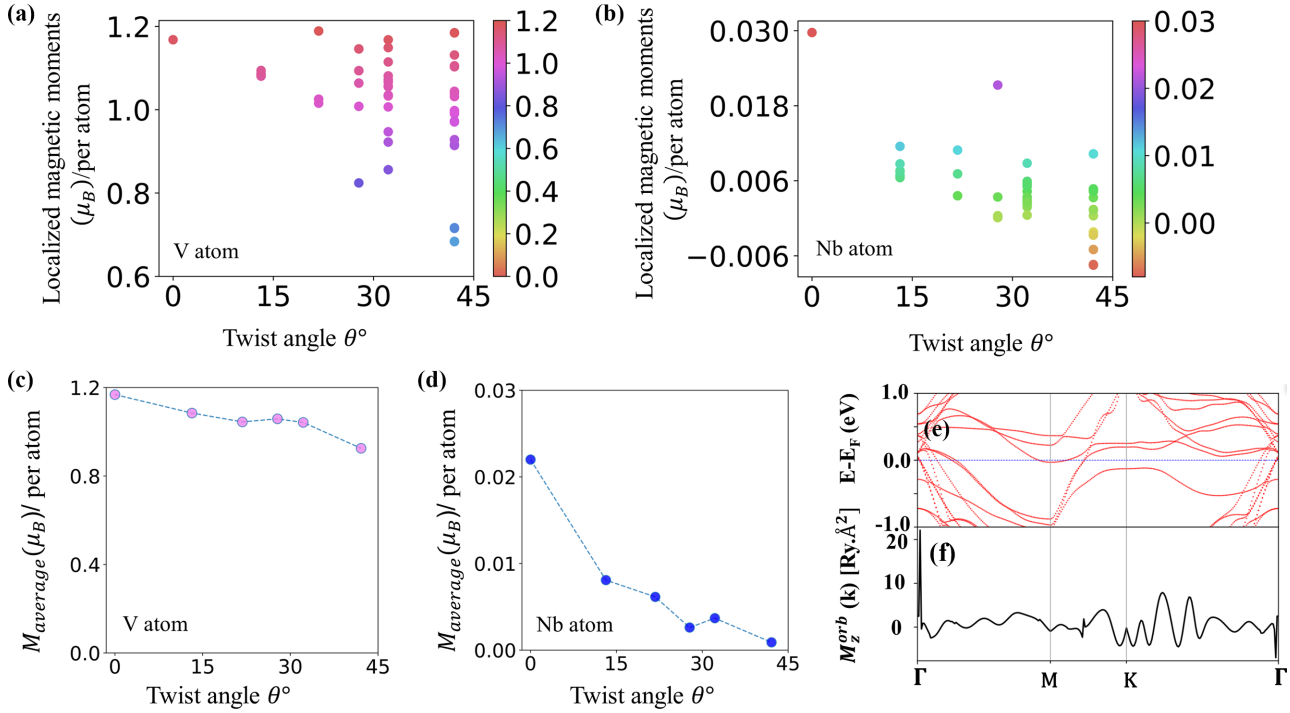

FIG. 5. Display of twist modified inhomogeneous local magnetization, average magnetic moment per atom, and orbital magnetism in studied systems. (a), (b) variation of localized magnetic moments per vanadium (V) atoms and niobium (Nb) atoms as a function of twist angles, (c), (d) average magnetic moment ($M_{average}$) per atom with respect to twist angles and (e), (f) electronic motion as well as orbital magnetism spread along the $\Gamma - M - K - \Gamma$ path of twist free unit cell in the Brillouin zone. The color boxes correspond to induced local moments at twist angle 0°, 13.17°, 21.79°, 27.80°, 32.20°, and 42.11°, respectively.

and 5(b) reveal twist angle dependent inhomogenous distribution of induced local moments at various twisted geometries of the vdW 1T-$NbSe_2$/1T-VSe_2 heterobilayer. Here, each dot represents localized moments generated during spin polarization calculations. Clear appearance of nonuniform local moments with varying strength (indicated in corresponding color boxes) is noticed as we increase the rotational angle between $NbSe_2$ and VSe_2 monolayers. Moreover, each local moment of V and Nb displays an inhomogeneous combination of quenched and augmented moments upon twisting. The degree of inhomogeneity in the magnetic moment per V atom is strongly influenced by the twist angles, depicting a significant variation of the variance of the magnetic moments with twist angles. A similar case for the $NbSe_2$ monolayer is also identified. This must be related to orbital rehybridization in moiré unit cells. At large twist angles, flattening of the bands [Fig. 3(h)] that makes the system more localizedlike allows for an inhomogeneous behavior. On the other hand, it is demonstrated that local magnetic moments emerging in twisted geometries of metal 1T-$NbSe_2$/1T-VSe_2 heterobilayers can be tuned as a function of twist angles. The variation of average magnetic moment $M_{average}$ per transition metal atoms with twist angles in Figs. 5(c) and 5(d) further supports the twist tunable magnetism in studied systems. We observe moderate dependency of average magnetic moments per atom at various twist angles.

As we have found, the nature of magnetism is an itinerant type; for cases of metallic or itinerant magnets, orbital magnetism has an essential role and is discussed in Figs. 5(e) and (f). Incorporating maximally localized Wannier function (MLWF) approach in the nontwisted unit cell, we calculate orbital magnetization the along easy (Z) axis. The obtained $M_z^{\mathrm{orb}} = 0.0197\,\mu_B$ per unit cell suggests the presence of orbital magnetism, but it is not as dominating as spin moments (1 μ_B/cell). Figure 5(e) unveils a band diagram of unit cells, and Fig. 5(f) depicts corresponding orbital magnetization distribution along the path $\Gamma - M - K - \Gamma$ in the Brillouin zone. The positive valued sharp peaks appear near Γ points when high energy region conduction bands are in contact with low lying energy level valance bands, and negative value of M_z^{orb} occurs in contactless regions of bands (here near k points) in k space [78]. Here, Nb and V atoms' spin and orbital contributions to magnetism are recognized. A plot for total magnetism in twist free and twisted unit cells, with respect to twist angles, is attached in Fig. S9 of the Supplemental Material [57].

IV. SUMMARY

In our study, we demonstrate the ability to control local magnetic moments and electron localization in a two-dimensional vdW $NbSe_2$-VSe_2 quantum material through twisting. The moiré superlattices lose localized magnetic moment homogeneity due to atomic orbital rehybridization resulting from the reconstruction of atoms in twisted cells. We find the effect of the twist angle on the total magnetic moment is negligible; rather, it has significant effect in local magnetic moments corresponding to constituent monolayers. All examined configurations fulfill the Stoner criteria of ferromagnetism, and the nonmagnetic trigonal phase of $NbSe_2$ monolayer develops a weak ferromagnetic ordering in vdW conjunction with VSe_2 monolayer for all investigated configurations. Overall, the process of orbital hybridization is not solely responsible for the creation of tailored magnetic moments, but also significantly impacts the electronic properties of the $NbSe_2$-VSe_2 vdW moiré magnet. The presence of narrow energy widths along with well-defined sharp density peaks in the DOS plot is indicative of strong electronic correlations in twisted structures. Prominent flat bands at twist angle 27.80° display robust electron localizations in transition metal atoms' $d_{x^2-y^2}$, d_{z^2} and d_{xy} orbitals near the Fermi level. On the other hand, the chalcogen atoms have minimal contribution toward flattened energy bands, indicating weak interlayer coupling effect. Apart from coexisting tunable itinerant ferromagnetism and flat bands in the studied crystals, evidence of orbital magnetism contributed by both Nb and V atoms is also found. The developed system provides a unique platform where three significant characteristics of electronic correlations are at play. In light of the cooccurrence of orbital and spin magnetism with flat bands, our results suggest that the proposed system may be useful for multifunctional applications in twistronics, spintronics, and electronic devices.

ACKNOWLEDGMENTS

S.M. and P.D. are grateful to the Indian Institute of Technology Kharagpur for providing the Supercomputing facility, set up under the National Supercomputing Mission (NSM), Govt. of India by the Centre for Development of Advanced Computing (CDAC), Pune. A special thanks to Liyenda Gogoi and Anil Kumar Singh for productive scientific discussions.

[1] E. Y. Andrei, D. K. Efetov, P. Jarillo-Herrero, A. H. MacDonald, K. F. Mak, T. Senthil, E. Tutuc, A. Yazdani, and A. F. Young, Nat. Rev. Mater. **6**, 201 (2021).

[2] Z. Hennighausen and S. Kar, Electron. Struct. **3**, 014004 (2021).

[3] L. Cai and G. Yu, Adv. Mater. **33**, 2004974 (2021).

[4] Y. Cao, V. Fatemi, S. Fang, K. Watanabe, T. Taniguchi, E. Kaxiras, and P. Jarillo-Herrero, Nature (London) **556**, 43 (2018).

[5] X. Ni, K. Chen, M. Weiner, D. J. Apigo, C. Prodan, A. Alu, E. Prodan, and A. B. Khanikaev, Commun. Phys. **2**, 55 (2019).

[6] C. R. Dean, L. Wang, P. Maher, C. Forsythe, F. Ghahari, Y. Gao, J. Katoch, M. Ishigami, P. Moon, M. Koshino *et al.*, Nature (London) **497**, 598 (2013).

[7] B. Hunt, J. D. Sanchez-Yamagishi, A. F. Young, M. Yankowitz, B. J. LeRoy, K. Watanabe, T. Taniguchi, P. Moon, M. Koshino, P. Jarillo-Herrero *et al.*, Science **340**, 1427 (2013).

[8] M. Yankowitz, S. Chen, H. Polshyn, Y. Zhang, K. Watanabe, T. Taniguchi, D. Graf, A. F. Young, and C. R. Dean, Science **363**, 1059 (2019).

[9] A. L. Sharpe, E. J. Fox, A. W. Barnard, J. Finney, K. Watanabe, T. Taniguchi, M. Kastner, and D. Goldhaber-Gordon, Science **365**, 605 (2019).

[10] J. H. Pixley and E. Y. Andrei, Science **365**, 543 (2019).

[11] H. Polshyn, J. Zhu, M. A. Kumar, Y. Zhang, F. Yang, C. L. Tschirhart, M. Serlin, K. Watanabe, T. Taniguchi, A. H. MacDonald *et al.*, Nature (London) **588**, 66 (2020).

[12] X. Lu, P. Stepanov, W. Yang, M. Xie, M. A. Aamir, I. Das, C. Urgell, K. Watanabe, T. Taniguchi, G. Zhang *et al.*, Nature (London) **574**, 653 (2019).

[13] J. Liu and X. Dai, Nat. Rev. Phys. **3**, 367 (2021).

[14] K. Hejazi, Z.-X. Luo, and L. Balents, Proc. Natl. Acad. Sci. USA **117**, 10721 (2020).

[15] X. Huang, T. Wang, S. Miao, C. Wang, Z. Li, Z. Lian, T. Taniguchi, K. Watanabe, S. Okamoto, D. Xiao *et al.*, Nat. Phys. **17**, 715 (2021).

[16] H. Pan and S. D. Sarma, Phys. Rev. Lett. **127**, 096802 (2021).

[17] X. Wang, C. Xiao, H. Park, J. Zhu, C. Wang, T. Taniguchi, K. Watanabe, J. Yan, D. Xiao, D. R. Gamelin *et al.*, Nature (London) **604**, 468 (2022).

[18] M. Akram, H. LaBollita, D. Dey, J. Kapeghian, O. Erten, and A. S. Botana, Nano Lett. **21**, 6633 (2021).

[19] C.-K. Li, X.-P. Yao, and G. Chen, Phys. Rev. Res. **3**, 033156 (2021).

[20] Y.-H. Li and R. Cheng, Phys. Rev. B **102**, 094404 (2020).

[21] M. Akram and O. Erten, Phys. Rev. B **103**, L140406 (2021).

[22] J. May-Mann and T. L. Hughes, Phys. Rev. B **101**, 245126 (2020).

[23] F. Xiao, K. Chen, and Q. Tong, Phys. Rev. Res. **3**, 013027 (2021).

[24] S. Ray and T. Das, Phys. Rev. B **104**, 014410 (2021).

[25] T. Song, Q.-C. Sun, E. Anderson, C. Wang, J. Qian, T. Taniguchi, K. Watanabe, M. A. McGuire, R. Stöhr, D. Xiao *et al.*, Science **374**, 1140 (2021).

[26] F. Zheng, Adv. Funct. Mater. **33**, 2206923 (2023).

[27] D. Ghader, Sci. Rep. **10**, 15069 (2020).

[28] Z. Lin, B. Huang, K. Hwangbo, Q. Jiang, Q. Zhang, Z. Liu, Z. Fei, H. Lv, A. Millis, M. McGuire *et al.*, Nano Lett. **21**, 9180 (2021).

[29] J. Shang, X. Tang, X. Tan, A. Du, T. Liao, S. C. Smith, Y. Gu, C. Li, and L. Kou, ACS Applied Nano Materials **3**, 1282 (2020).

[30] K. Dong, T. Zhang, J. Li, Q. Wang, F. Yang, Y. Rho, D. Wang, C. P. Grigoropoulos, J. Wu, and J. Yao, Phys. Rev. Lett. **126**, 223601 (2021).

[31] Z. Zhang, Y. Wang, K. Watanabe, T. Taniguchi, K. Ueno, E. Tutuc, and B. J. LeRoy, Nat. Phys. **16**, 1093 (2020).

[32] H. Huang, L. Zheng, Z. Lin, X. Guo, S. Wang, S. Zhang, C. Zhang, Z. Sun, Z. Wang, H. Weng *et al.*, Phys. Rev. Lett. **128**, 096601 (2022).

[33] Y.-W. Liu, J.-B. Qiao, C. Yan, Y. Zhang, S.-Y. Li, and L. He, Phys. Rev. B **99**, 201408(R) (2019).

[34] K. Yamagami, Y. Fujisawa, B. Driesen, C.-H. Hsu, K. Kawaguchi, H. Tanaka, T. Kondo, Y. Zhang, H. Wadati, K. Araki *et al.*, Phys. Rev. B **103**, L060403 (2021).

[35] J. Finney, A. L. Sharpe, E. J. Fox, C. L. Hsueh, D. E. Parker, M. Yankowitz, S. Chen, K. Watanabe, T. Taniguchi, C. R. Dean *et al.*, Proc. Natl. Acad. Sci. USA **119**, e2118482119 (2022).

[36] A. Lopez-Bezanilla, Phys. Rev. Mater. **3**, 054003 (2019).

[37] J.-X. Yin, S. S. Zhang, G. Chang, Q. Wang, S. S. Tsirkin, Z. Guguchia, B. Lian, H. Zhou, K. Jiang, I. Belopolski *et al.*, Nat. Phys. **15**, 443 (2019).

[38] M. Bora, S. K. Behera, P. Samal, and P. Deb, Phys. Rev. B **105**, 235422 (2022).

[39] A. Kerelsky, L. J. McGilly, D. M. Kennes, L. Xian, M. Yankowitz, S. Chen, K. Watanabe, T. Taniguchi, J. Hone, C. Dean *et al.*, Nature (London) **572**, 95 (2019).

[40] S.-y. Li, Z. Wang, Y. Xue, Y. Wang, S. Zhang, J. Liu, Z. Zhu, K. Watanabe, T. Taniguchi, H.-j. Gao *et al.*, Nat. Commun. **13**, 4225 (2022).

[41] X.-J. Zhao, Y. Yang, D.-B. Zhang, and S.-H. Wei, Phys. Rev. Lett. **124**, 086401 (2020).

[42] E. C. Regan, D. Wang, C. Jin, M. I. Bakti Utama, B. Gao, X. Wei, S. Zhao, W. Zhao, Z. Zhang, K. Yumigeta *et al.*, Nature (London) **579**, 359 (2020).

[43] Y. Nakata, K. Sugawara, R. Shimizu, Y. Okada, P. Han, T. Hitosugi, K. Ueno, T. Sato, and T. Takahashi, NPG Asia Materials **8**, e321 (2016).

[44] M. Bonilla, S. Kolekar, Y. Ma, H. C. Diaz, V. Kalappattil, R. Das, T. Eggers, H. R. Gutierrez, M.-H. Phan, and M. Batzill, Nat. Nanotechnol. **13**, 289 (2018).

[45] P. M. Coelho, K. Nguyen Cong, M. Bonilla, S. Kolekar, M.-H. Phan, J. Avila, M. C. Asensio, I. I. Oleynik, and M. Batzill, J. Phys. Chem. C **123**, 14089 (2019).

[46] K. Sumida, Y. Takeda, S. Kusaka, K. Kobayashi, and T. Hirahara, Phys. Rev. Mater. **6**, 014006 (2022).

[47] B. Marfoua and J. Hong, Commun. Phys. **5**, 266 (2022).

[48] S. Kezilebieke, M. N. Huda, P. Dreher, I. Manninen, Y. Zhou, J. Sainio, R. Mansell, M. M. Ugeda, S. van Dijken, H.-P. Komsa *et al.*, Commun. Phys. **3**, 116 (2020).

[49] T. Yilmaz, X. Tong, Z. Dai, J. T. Sadowski, E. F. Schwier, K. Shimada, S. Hwang, K. Kisslinger, K. Kaznatcheev, E. Vescovo *et al.*, Commun. Mater. **2**, 11 (2021).

[50] Z. Zhang, Y. Gong, X. Zou, P. Liu, P. Yang, J. Shi, L. Zhao, Q. Zhang, L. Gu, and Y. Zhang, ACS Nano **13**, 885 (2019).

[51] T. G. Park, B. K. Choi, J. Park, J. Kim, Y. J. Chang, and F. Rotermund, ACS Nano **15**, 7756 (2021).

[52] W. Yang, Y. Cao, J. Han, X. Lin, X. Wang, G. Wei, C. Lv, A. Bournel, and W. Zhao, Nanoscale **13**, 862 (2021).

[53] J.-Q. Dai, J. Yuan, C. Ke, and Z.-C. Wei, Appl. Surf. Sci. **547**, 149206 (2021).

[54] F. Kadijk and F. Jellinek, J. Less-Common Met. **23**, 437 (1971).

[55] P. Giannozzi, S. Baroni, N. Bonini, M. Calandra, R. Car, C. Cavazzoni, D. Ceresoli, G. L. Chiarotti, M. Cococcioni, I. Dabo *et al.*, J. Phys.: Condens. Matter **21**, 395502 (2009).

[56] G. Prandini, A. Marrazzo, I. E. Castelli, N. Mounet, and N. Marzari, npj Comput. Mater. **4**, 72 (2018).

[57] See Supplemental Material at http://link.aps.org/supplemental/10.1103/PhysRevB.108.054433 for details related to number atoms, moire lattice constant, Stoner criterion analysis, work functions, and total magnetic moment evolution with twist angle for a particular pair of (n, m).

[58] A. A. Mostofi, J. R. Yates, Y.-S. Lee, I. Souza, D. Vanderbilt, and N. Marzari, Comput. Phys. Commun. **178**, 685 (2008).

[59] Q. Wu, S. Zhang, H.-F. Song, M. Troyer, and A. A. Soluyanov, Comput. Phys. Commun. **224**, 405 (2018).

[60] I. Petousis, D. Mrdjenovich, E. Ballouz, M. Liu, D. Winston, W. Chen, T. Graf, T. D. Schladt, K. A. Persson, and F. B. Prinz, Sci. Data **4**, 1 (2017).
[61] E. Cisternas, M. Flores, and P. Vargas, Phys. Rev. B **78**, 125406 (2008).
[62] J. M. Campanera, G. Savini, I. Suarez-Martinez, and M. I. Heggie, Phys. Rev. B **75**, 235449 (2007).
[63] F. Conte, D. Ninno, and G. Cantele, Phys. Rev. B **99**, 155429 (2019).
[64] E. J. Mele, Phys. Rev. B **81**, 161405 (2010).
[65] P. Moon and M. Koshino, Phys. Rev. B **85**, 195458 (2012).
[66] P. de Silva and C. Corminboeuf, J. Chem. Theory Comput. **10**, 3745 (2014).
[67] Z.-L. Liu, X. Wu, Y. Shao, J. Qi, Y. Cao, L. Huang, C. Liu, J.-O. Wang, Q. Zheng, Z.-L. Zhu *et al.*, Sci. Bull. **63**, 419 (2018).
[68] L. Xu, W.-Q. Huang, W. Hu, K. Yang, B.-X. Zhou, A. Pan, and G.-F. Huang, Chem. Mater. **29**, 5504 (2017).
[69] M. Ashwin Kishore, K. Larsson, and P. Ravindran, ACS Omega **5**, 23762 (2020).
[70] M. Aras, Ç. Kılıç, and S. Ciraci, Phys. Rev. B **101**, 054429 (2020).
[71] J. Kübler, *Theory of Itinerant Electron Magnetism*, Vol. 106 (Oxford University Press, Oxford, 2017).
[72] P. M. Marcus and V. L. Moruzzi, Phys. Rev. B **38**, 6949 (1988).
[73] J. Attig, J. Park, M. M. Scherer, S. Trebst, A. Altland, and A. Rosch, 2D Mater. **8**, 044007 (2021).
[74] Q. Xu, Y. Guo, and L. Xian, 2D Mater. **9**, 014005 (2022).
[75] A. Weston, Y. Zou, V. Enaldiev, A. Summerfield, N. Clark, V. Zólyomi, A. Graham, C. Yelgel, S. Magorrian, M. Zhou *et al.*, Nat. Nanotechnol. **15**, 592 (2020).
[76] H. Zheng, B. Wu, S. Li, J. He, K. Chen, Z. Liu, and Y. Liu, Nano Res. **16**, 3429 (2023).
[77] V. V. Enaldiev, V. Zolyomi, C. Yelgel, S.J. Magorrian, and V. I. Fal'Ko, Phys. Rev. Lett. **124**, 206101 (2020).
[78] M. G. Lopez, D. Vanderbilt, T. Thonhauser, and I. Souza, Phys. Rev. B **85**, 014435 (2012).